

2022

A figure of merit to characterize the efficacy of evaporation from porous microstructured surfaces

M. Bongarala

H. Hu

J.A. Weibel

S.V. Garimella

Follow this and additional works at: <https://docs.lib.purdue.edu/coolingpubs>

Bongarala, M.; Hu, H.; Weibel, J.A.; and Garimella, S.V., "A figure of merit to characterize the efficacy of evaporation from porous microstructured surfaces" (2022). *CTRC Research Publications*. Paper 390. <http://dx.doi.org/10.1016/j.ijheatmasstransfer.2021.121964>

This document has been made available through Purdue e-Pubs, a service of the Purdue University Libraries. Please contact epubs@purdue.edu for additional information.

A Figure of Merit to Characterize the Efficacy of Evaporation from Porous Microstructured Surfaces

Manohar Bongarala ^a, Han Hu ^b, Justin A. Weibel ^{a,1}, and Suresh V. Garimella ^{a,c}

^a School of Mechanical Engineering and Birck Nanotechnology Center, Purdue University, West
Lafayette, IN 47907 USA

^b Department of Mechanical Engineering, University of Arkansas, Fayetteville, AR 72701 USA

^c University of Vermont, Burlington, VT 05405 USA

ABSTRACT

Evaporation from porous structured surfaces is encountered in a variety of applications including electronics cooling, desalination, and solar energy generation. Of major interest in the design of thermal systems for such applications is a prediction of the heat and mass transfer rates during evaporation from these surfaces. The present study develops a figure of merit (FOM) that characterizes the efficacy of evaporative heat transfer from microstructured surfaces. Geometric quantities such as the contact line length per unit area, porosity, and contact angle that are independent of details of the surface structure are utilized to develop the FOM, allowing for flexibility in its application to a variety of structured surfaces. This metric is calibrated against an evaporative heat transfer model and further benchmarked with evaporation heat transfer data from the literature. The FOM successfully captures the variation in evaporation heat transfer coefficient across different structures as well as the optimum dimensions for a given structure, and therefore can serve as a tool to survey available structures and also optimize their dimensions for heat and mass transfer enhancement.

Keywords: thin-film evaporation; structured surfaces; microstructures; thermal performance; two-phase cooling.

¹ Corresponding author. E-mail: jaweibel@purdue.edu (J.A. Weibel)

Nomenclature

A	area, m^2
A_{fp}	footprint area, m^2
A_m	effective area for conduction between liquid-vapor interface and solid-liquid interface, m^2
D	diameter, m
FOM	figure of merit
H_{ch}	characteristic liquid film height, m
H_{ch0}	characteristic liquid film height from the projection of the meniscus, m
h	height of liquid meniscus, m
h_{eff}	overall evaporation heat transfer coefficient, $W/(m^2 \cdot K)$
h_{evap}	evaporation heat transfer coefficient, $W/(m^2 \cdot K)$
h_{fg}	enthalpy of vaporization, J/kg
k_l	liquid thermal conductivity, $W/(m \cdot K)$
l_{ch}	relevant length scale for evaporation, m
M	molar mass, kg/mol
P	pitch, m
P^*	effective pitch, m
q''	heat flux, $W \text{ cm}^{-2}$
q''_{eff}	overall heat flux from structured surface, $W \text{ cm}^{-2}$
R^*	radius of curvature of the meniscus, m
R_{cond}	thermal conduction resistance due to the liquid film, K/W
R_{eff}	effective resistance from the base of the microstructure to the top, K/W
R_{evap}	thermal resistance due to interfacial evaporation, K/W
R_u	universal gas constant, J/mol-K
S	spacing between the structures, m
δ_{ch0}	characteristic liquid film thickness from projection of the meniscus, m
T_{lv}	liquid-vapor interface temperature, K
T_v	vapor temperature, K
T_w	wall/microstructure temperature, K
u_r	radial flow velocity, m/s
w	width, m
<i>Greek</i>	

$\Delta\rho_{lv}$	difference in liquid and vapor density, kg/m ³
ΔT	superheat ($T_w - T_v$), K
$\delta(y)$	thickness of the liquid between the structure and liquid-vapor interface at a particular height, m
δ_{c0}	critical film thickness, m
δ_{ch}	characteristic liquid film thickness, m
ε	area-based porosity
μ	dynamic viscosity, m ² /s
θ	contact angle, rad
$\hat{\sigma}$	accommodation coefficient
<i>Subscripts</i>	
ch	characteristic quantities
cond	quantity at the solid-liquid interface
e	evaporation
eff	effective properties
evap	quantity at the liquid-vapor interface
pillar	quantity corresponding to a pillar structure
pore	quantity corresponding to a pore structure
sq	quantity corresponding to a square array structure

1. Introduction

Evaporation plays a central role in several applications including energy conversion [1–3], steam generation [4,5], desalination [6], self-assembly [7], and electronics cooling. The last of these applications encounters serious challenges as the performance and efficiency of modern logic processors, power amplifier devices, and other integrated circuits is limited by the ability to effectively dissipate the heat generated inside these components. In particular, high heat fluxes must be dissipated through small device footprint areas. The energy absorbed as latent heat by liquid-vapor phase change during evaporation offers one of the most promising cooling solutions. Phase-change-based thermal management technologies such as immersion cooling [8], jet impingement [9], and microchannel flow boiling [10] all involve evaporation processes. Understanding these processes, as well as developing tools for predicting and enhancing evaporation heat transfer, is key to designing cooling technologies involving liquid-vapor phase change.

Early studies of evaporation transport considered thin-film menisci formed in small capillary tubes, with notable contributions by Derjagin et al. [11]. Since then, the fundamentals of phase change transport in thin films have been extensively investigated using theoretical [12–15], experimental [16–18], and numerical methods [19,20]. For a heated surface covered with an evaporating liquid film, heat from the solid substrate is conducted through the bulk of the liquid and then rejected via phase change at the liquid-vapor interface. Over a majority of the film surface, evaporation is suppressed by the high thermal resistance offered by the bulk liquid. For a wetting liquid, much of the evaporation occurs from a thin-film region (also called transition region) due to the low thermal resistance of the film in this region, and also a weaker molecular attraction to the solid surface than in the much smaller absorbed-film region closest to the solid-liquid-vapor triple line. To exploit thin-film evaporation, systems are designed to enhance the area of the liquid-vapor interface that is in close proximity to the heating surface (film thickness on the order of microns), with low thermal resistance and high evaporation flux [21]. The use of micro-/nano-structured surfaces helps to further increase the available thin-film area for evaporation so as to enhance the effective heat transfer coefficient.

Phase change from microstructured surfaces offers two major advantages: (i) avoidance of surface dryout; and (ii) enhancement in the heat transfer coefficient. The microscale gaps between

the microstructures allow the surface to wick or imbibe liquid by capillary action, ensuring that it is wetted with liquid while the phase change process dissipates heat. At a certain heat flux, capillarity becomes insufficient to maintain the required rate of liquid feeding, causing dryout. This phenomenon leads to failure in devices like heat pipes and vapor chambers, and has therefore attracted much attention especially with respect to transport in wick structures [22–25].

Another crucial role of microstructuring is to increase the number of liquid menisci per unit footprint area, and thus increase the total length of the three-phase contact line over which strong thin-film evaporation occurs. This leads to an increase in the thin-film evaporation area and thereby the overall effective heat transfer coefficient. In order to design optimal microstructures to enhance evaporation, it is important to understand the influence of morphological parameters on the heat transfer coefficient. Several prior works have studied the influence of microstructuring on the effective evaporative heat transfer coefficient [25–32].

Hanlon and Ma [25] explored the dryout heat flux and heat transfer coefficient during evaporation from a sintered copper wick. An analytical model based on thin-film evaporation at the top surface coupled with hydrodynamic modeling for flow was used to predict the heat transfer capability of wicks. Supported by experiments using wicks of different thicknesses, wick properties such as particle size, porosity, thickness were found to play an important role in the enhancement of evaporative heat transfer. Simulations of evaporation from liquid menisci formed in different wick structures have also been conducted in the literature to assess their heat transfer performance. In a study by Ranjan et al. [26], four wick geometries (horizontal wires, vertical wires, square packed spheres, and rectangular ribs) were compared. The simulations first determined a fixed interface shape using energy minimization. The conductive and convective heat transfer in the fluid domain was then simulated numerically using a finite volume approach. The simulations captured phase change at the liquid-vapor interface using Schrage's expression for evaporated mass flux [33]. Based on the simulations, the contribution of Marangoni convection inside the structures was concluded to be negligible compared to the conduction heat transfer; packed spheres showed the highest rate of evaporation out of the four different geometries studied. The work also explored the influence of contact angle, surface superheat, porosity, and wire diameter on heat transfer coefficient for horizontal wires. Ranjan et al. [27] also explored novel micropillared, pyramidal, and conical structures for application in thin vapor chambers. A permeability model for simulating the flow through these structures was developed in conjunction

with the evaporation model to compare both the hydrodynamic and evaporative performance of the novel wicks. Pyramidal wick structures were found to outperform other wicks in terms of capillary pressure generated as well as the evaporation rate. Bodla et al. [28] numerically estimated the thin-film evaporation from real sintered particle samples reconstructed using X-ray microtomography. For a given porous structure, the steady shape of the liquid meniscus was obtained by an unsteady volume-of-fluid approach, and a heat transfer analysis following the approach of Ranjan et al. [26] was performed by fixing the meniscus at the steady shape. The evaporation mass flux was found to increase with a decrease in contact angle and particle size. This effective increase was attributed to the increase in the overall meniscus area.

Highly ordered microstructures based on silicon photolithography have also been used to study evaporation. Farokhnia et al. [29] explored the influence of geometric parameters on the evaporative heat transfer coefficient from three different structures. Square pillars, circular pillars, and rectangular ribs were analytically modelled assuming conduction as the heat transfer pathway from the solid structure to the evaporating interface of constant curvature. The work explored the optimum structure geometric parameters for maximizing the heat transfer coefficient enhancement and found the optimal width-to-spacing ratios for rectangular ribs. They fabricated and experimentally measured the evaporation heat flux from square pillar arrays to validate their model. Adera et al. [30] experimentally characterized capillary-limited thin-film evaporation from silicon micropillar arrays. Dryout heat fluxes and superheats were measured experimentally for different micropillared surfaces and were shown to agree well with an analytical model. The model consisted of a liquid flow prediction using the Brinkman equation and a superheat prediction using an effective thermal network resistance model.

Researchers have also explored the use of novel microstructures that aim to enhance evaporation by increasing the thin-film region by designing the curvature of the solid surface. Montazeri et al. [31] performed 2D conduction simulations to explore the influence of pore size on the evaporation heat transfer coefficient performance of cylindrical grooves. The results showed a decrease in evaporation performance with an increase in contact angle and the pore diameter. Bang et al. [32] introduced superhydrophilic aluminum catenoidal structures for evaporator wicks. The heat transfer coefficient from these structures was experimentally found to be ~117% higher than cylindrical structures. The experimental study was also complemented with predictions of

evaporation by performing simulations of liquid-filled structures using numerical approaches similar to those discussed above.

This review establishes that the modeling of the evaporation heat transfer coefficient from structured surfaces follows either high-fidelity conjugate numerical simulations or thermal conduction modeling, and the approaches agree well with each other [26]. These modeling approaches have limited utility, however, for surveying the performance of different surface structures, as a simulation is required to evaluate each specific geometry while searching for an optimum morphology. There is a need for lower-order modeling approaches that can quickly assess microstructured surfaces of any generalized morphology for enhancing the heat transfer coefficient during evaporation.

In the present work, we develop a figure of merit (FOM) that serves as a simple metric to evaluate the evaporative heat flux from structured surfaces. Rather than requiring a model of the structure geometry, the FOM includes only effective parameters such as porosity, three-phase contact line length per unit area, and contact angle, and hence is structure-agnostic. The FOM can serve as a tool for surveying and deciding between surface morphologies in a large search domain across various applications. In the sections that follow, an effective evaporation model is first developed for purposes of calibration of the FOM by comparing the evaporation heat fluxes of three basic geometries: a hexagonal pillar array, square pillar array, and square cylindrical pore array. The FOM is then subsequently developed by simplifying and scaling the 3-D meniscus to a uniform film of constant thickness. The FOM is compared against data in the literature for various structured surfaces, establishing its validity as a tool for accurately predicting the relative performance between structures. Lastly, the FOM formulation is analyzed to obtain insight into the design objective for maximizing the evaporative heat transfer coefficient.

2. Modeling Approach

Evaporation from a structured surface is a multifaceted phenomenon involving phase change, capillary wicking, conduction, and convection. For a given structured surface, the heat transfer coefficient depends not only on its morphology, but also on the ambient conditions, fluid properties, liquid feeding, and other factors. To isolate the effect of surface morphology on the heat transfer coefficient for purposes of developing a figure of merit, appropriate assumptions and boundary conditions are used to suppress these other influences on evaporation. The ambient vapor

pressure, as well as advection and diffusion in the surrounding gas domain, can critically influence phase change and hence the evaporative performance of the surface under unsaturated vapor conditions [34]. Hence, a saturated pure vapor environment is considered for the modeling, which is representative of most applications and eliminates the influence of the gas domain. Liquid feeding through the structure also plays an important role in maintaining evaporation. To maintain a mass balance during evaporation, liquid is replenished by capillary action to maintain a steady meniscus profile. While insufficient feeding could trigger a change in the meniscus shape, leading to a coupling between liquid wicking and evaporation [30], for the present study, the structure is assumed to be well-fed with liquid such that the liquid meniscus inside the structures is static.

Liquid in between the structures develops a temperature gradient due to heating from the substrate below and/or evaporative cooling at the interface that can induce convective currents. It has been shown in past work that the contribution of advection heat transfer is negligible compared with conduction to the evaporating interface [26]. Therefore, convection inside the liquid is neglected, and conduction is considered as the sole mechanism of heat transfer through the liquid to the evaporating interface. The heat rejection pathway thereby occurs via conduction through the solid structures, conduction through the liquid, and then evaporation at the liquid-vapor interface. The resistance to conduction through the solid is comparatively small and is neglected under the assumption that the conductivity of the solid structures is large. For high-aspect-ratio or low-conductivity structures that develop a thermal gradient along their height, an additional conduction resistance could be trivially included.

2.1 Evaporation model

In this subsection, an evaporation model is developed to predict the heat flux for three typical surface structure morphologies: circular pillars (hexagonal array), circular pillars (square array), and cylindrical pores (square array). Consider the unit cell of a regularly repeating solid surface structure and liquid meniscus shown in Figure 1. The structure shown in this figure is sketched for a representative geometry, and could be assumed as a pore to facilitate understanding, although the derivation that follows is presented in general terms and is applicable for each of the different structures considered. As previously discussed, the heat rejection occurs from solid to the liquid-vapor interface, followed by evaporation to the saturated vapor ambient. Considering a differential

element along the meniscus, as shown on the right side of Figure 1, and applying conservation of energy

$$q''_{\text{cond}} dA_{\text{cond}} = q''_{\text{evap}} dA_{\text{evap}} \quad (1)$$

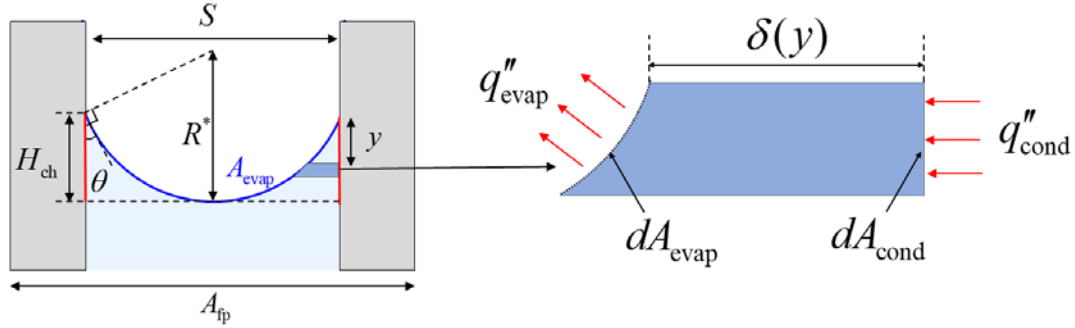


Figure 1. Schematic drawing that depicts the shape of the meniscus within a structured surface. The meniscus has a constant curvature with radius (R^*) and contact angle (θ). A differential element of the meniscus shows the thermal conduction pathway from the structure to the interface.

We assume the solid structure is at a uniform temperature T_w . The left-hand side of the above equation represents the heat entering the elemental control volume of liquid film located at a height y and of thickness $\delta(y)$. At steady state, the heat entering the control volume is conducted to the liquid-vapor interface and rejected via evaporation. Heat flow by conduction is given by

$$q''_{\text{cond}} dA_{\text{cond}} = \frac{(T_w - T_{lv}) k_l dA_m}{\delta(y)} \quad (2)$$

where δ and dA_m are respectively the film thickness and effective elemental area through which conduction occurs. The local evaporation heat at the liquid-vapor interface is given by

$$q''_{\text{evap}} = h_{\text{evap}} (T_{lv} - T_v) \quad (3)$$

The evaporation heat flux defined based on the footprint area A_{fp} of the unit cell is given by

$$q''_{\text{eff}} = \frac{\int_{A_{\text{evap}}} q''_{\text{evap}} dA_{\text{evap}}}{A_{fp}} \quad (4)$$

Neglecting the effects of convection inside the liquid, an energy balance on the control volume gives $q''_{\text{cond}} dA_{\text{cond}} = q''_{\text{evap}} dA_{\text{evap}}$. Eliminating T_{lv} using the energy balance and using Equations (2) to (4), the heat flux can be rewritten as

$$q''_{\text{eff}} = \frac{1}{A_{\text{fp}}} \int_{A_{\text{evap}}} \frac{h_{\text{evap}} \Delta T}{1 + (dA_{\text{evap}}/dA_{\text{cond}})(dA_{\text{cond}}/dA_{\text{m}})(\delta/\delta_{c0})} dA \quad (5)$$

Here $\Delta T = T_w - T_v$ is the superheat of the surface, $\delta_{c0} = k_1 / h_{\text{evap}}$ is the critical film thickness and the elemental areas dA_{evap} and dA_{cond} are described in Figure 1. The evaporation heat transfer coefficient at the liquid-vapor interface under saturation conditions is calculated as

$$h_{\text{evap}} = \frac{2\hat{\sigma}}{2-\hat{\sigma}} \frac{\rho_v h_{\text{fg}}^2}{T_v} \sqrt{\frac{M}{2\pi R_u T_v}} \quad (6)$$

The expression for the heat flux in Equation (5) is independent of the morphology of the structured surface and can be applied to the pillar and pore structures depicted in Figure 2. The meniscus around a pillar inside the pillar arrays is not axisymmetric. In order to simplify the problem, we assume each pillar in the array is surrounded by an axisymmetric meniscus of outer diameter P^*_{pillar} as shown in Figure 2 (a). These effective pitches are calculated by converting the footprint area to a radial domain from the square/hexagonal domain as depicted in Figure 2. For instance, for the square pillar array, the area occupied by the meniscus in a unit cell is $P_{\text{sq}}^2 - \pi D_{\text{pillar}}^2 / 4$ (Figure 2 (c)). This area is equated with the liquid-filled area in the effective meniscus in Figure 2 (a) to get P^*_{pillar} . Inserting the appropriate areas for either a square or hexagonal pillar array (Figure 2 (c,d)), an expression for the evaporation heat flux for the pillar geometries using Equation (5) is given by

$$q''_{\text{eff,pillar}} = \frac{4}{\pi P_{\text{pillar}}^{*2}} \int_0^{(P_{\text{pillar}}^* - D_{\text{pillar}})(1-\sin\theta)/(2\cos\theta)} \frac{2\pi (D_{\text{pillar}}/2 + \delta) \sqrt{1 + \delta'^2} h_{\text{evap}} \Delta T}{1 + \sqrt{1 + \delta'^2} (D_{\text{pillar}}/2 + \delta) \ln \left(\frac{D_{\text{pillar}}/2 + \delta}{D_{\text{pillar}}/2} \right) \frac{h_{\text{evap}}}{k_1}} dy \quad (7)$$

A similar expression can be derived for the pore geometry (Figure 2 (e)) using Equation (5)

$$q''_{\text{eff,pore}} = \frac{4}{\pi P_{\text{pore}}^{*2}} \int_0^{D_{\text{pore}}(1-\sin\theta)/(2\cos\theta)} \frac{2\pi \sqrt{1 + \delta'^2} (D_{\text{pore}}/2 - \delta) h_{\text{evap}} \Delta T}{1 + \sqrt{1 + \delta'^2} (D_{\text{pore}}/2 - \delta) \ln \left(\frac{D_{\text{pore}}/2}{D_{\text{pore}}/2 - \delta} \right) \frac{h_{\text{evap}}}{k_1}} dy \quad (8)$$

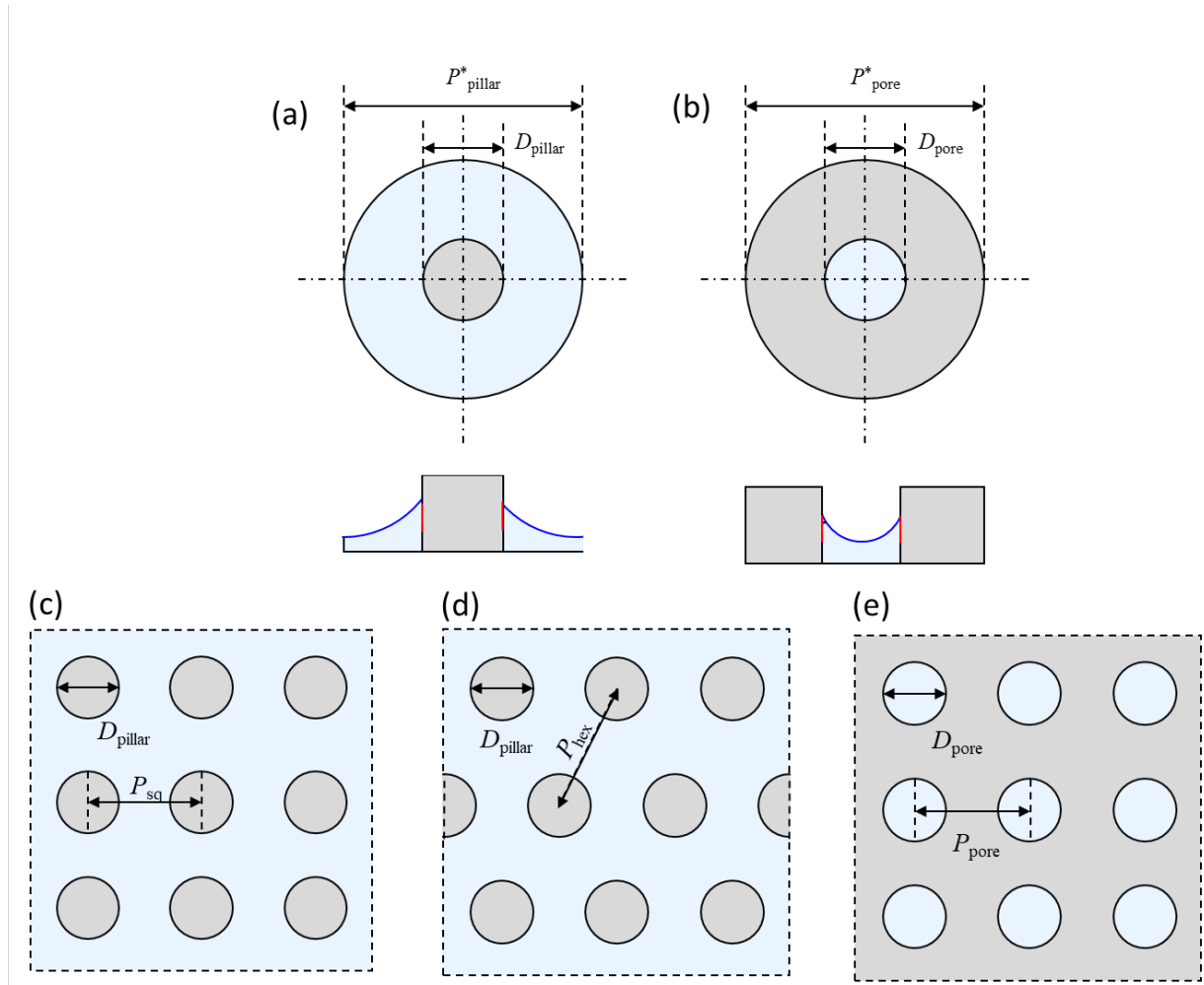


Figure 2. Schematic drawings of an evaporating meniscus (a) around a pillar and (b) in a pore. Top-down views are shown for (c) a square pillar array, (d) a hexagonal pillar array, and (e) a square pore array. The structures in the array (c-d) are transformed to axisymmetric unit cells represented in (a-b).

The above equations are valid for any generic shape of the meniscus $\delta(y)$. For the results presented in the current study, the meniscus is assumed to have a constant radius of curvature (R^*) and the above two equations are further simplified. The shape of the meniscus is a circular arc with the appropriate contact angle, rotated around the pillar. The integrals are solved numerically to obtain the heat fluxes and overall heat transfer coefficients as a function of the surface morphology and the superheat (ΔT).

2.2 Evaporation Figure of Merit (FOM)

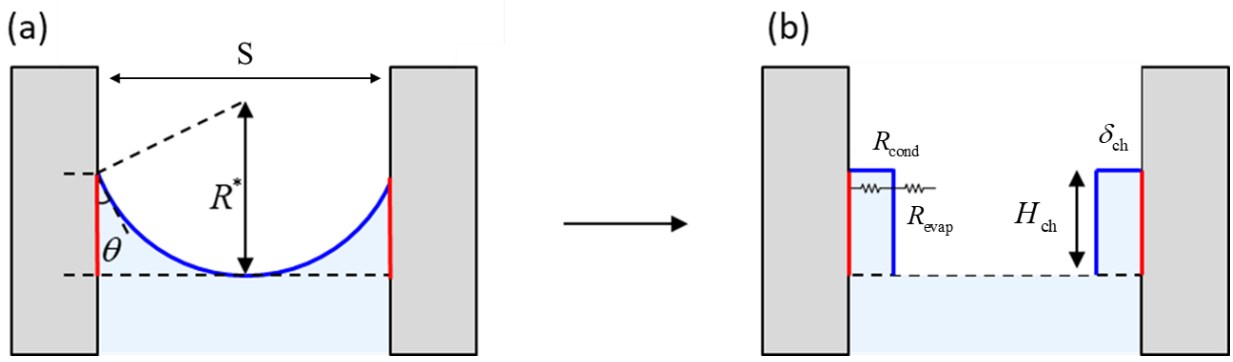


Figure 3. Schematic drawings depicting the simplification of the meniscus shape to develop the figure of merit. The meniscus shape used for (a) the evaporation model and (b) the simplification to a uniform thickness and height for deriving the figure of merit are shown.

The generic expression representing the evaporation heat flux (Equation (5)) developed in the previous section has limited utility as a performance metric due to its integral form and the geometrical complexity involved in calculating the differentials for a 3D meniscus. To derive an evaporation figure of merit (FOM), we assume that the meniscus is composed of a uniform liquid film that has a characteristic thickness δ_{ch} and height H_{ch} (as per the simplification depicted in Figure 3). Expressions for the characteristic thickness and height of the film, which depend on the specific structure, will be discussed after the introduction of the FOM. Per this simplification, heat is conducted from the solid to the interface through a uniform liquid film of thickness δ_{ch} and height H_{ch} . The evaporation figure of merit is defined as the non-dimensional heat flux from a given structured surface. The heat flux can be further decomposed into the thermal resistances to evaporation as

$$FOM = \frac{q_{eff}''}{h_{evap} \Delta T} = \frac{\left(\frac{\Delta T}{R_{cond} + R_{evap}} \right)}{h_{evap} A_{ip} \Delta T} \quad (9)$$

Based on the effective thin-film properties, the conduction resistance across the thin film is given by $R_{cond} = \delta_{ch} / (k_l H_{ch} L_{cl})$, where L_{cl} is the three-phase contact line length inside a unit cell and k_l is the thermal conductivity of the liquid. The interfacial evaporative resistance is given by $R_{evap} = 1 / (h_{evap} A_{evap})$. The figure of merit then becomes

$$FOM = \left\{ \left(\frac{h_{\text{evap}}}{k_1} \frac{\delta_{\text{ch}}}{H_{\text{ch}}} \frac{A_{\text{fp}}}{L_{\text{cl}}} \right) + \left(\frac{A_{\text{fp}}}{A_{\text{evap}}} \right) \right\}^{-1} \quad (10)$$

All the parameters involved in the evaporation figure of merit can be organized into relevant parameter groupings that govern the evaporative performance: (i) the three-phase contact line length per unit area ($L_{\text{cl}}/A_{\text{fp}}$), (ii) a thermophysical property constant (k_1/h_{evap}), (iii) the effective area of evaporation ($A_{\text{evap}}/A_{\text{fp}}$), and (iv) the characteristic dimensions of the liquid thin film ($\delta_{\text{ch}}/H_{\text{ch}}$). The figure of merit as defined does not incorporate the conduction resistance through the solid microstructures from the base of the surface. This resistance is negligible for the structures with very low aspect ratios in this work. For high aspect ratio structures, an extension of the FOM is offered in the supplemental material S1 that incorporates conduction resistance through the solid substrate.

The three-phase contact line length per unit area for a given morphology can be easily calculated with knowledge of the height of the meniscus (h). For example, for a square pillared structure, the contact line length in a unit cell is πD_{sq} and unit footprint area is P_{sq}^2 . Expressions for various other structures are depicted in Table 1. The thermophysical property constant is calculated based on the liquid thermal conductivity and h_{evap} .

The effective area of evaporation ($A_{\text{evap}}/A_{\text{fp}}$) is the area of the meniscus available for evaporation per unit footprint area. This is defined in terms of a two-dimensional porosity (ε) and the contact angle (θ). The two-dimensional porosity is defined as the ratio of projected liquid-filled area and the footprint area: $\varepsilon = A_{\text{proj}}/A_{\text{fp}}$. The meniscus area available for evaporation is greater than the projected liquid-filled area due to the meniscus curvature. To calculate this quantity, we broadly categorize the surface structures into two meniscus shapes, either 3D axisymmetric or 2D extruded. If the meniscus is close to axisymmetric (e.g., in the case of a pore/sphere array/ pillar array), the effective area is calculated based on a 3D spherical meniscus approximation: $\frac{A_{\text{evap}}}{A_{\text{fp}}} = \frac{2\varepsilon}{1 + \sin \theta}$. For cases having a 2D extruded meniscus, such as that in

rectangular ribs or horizontal wires, the enhancement is based on a cylindrical meniscus shape:

$$\frac{A_{\text{evap}}}{A_{\text{fp}}} = \frac{\varepsilon \left(\frac{\pi}{2} - \theta \right)}{\cos \theta}.$$

A scaling analysis is used to estimate the ratio of characteristic thin-film thickness (δ_{ch}) to height (H_{ch}) (see supplemental material S2 for the details of this analysis). The characteristic film thickness is at a scale of $\delta_{\text{ch}} \sim \left[(S/2)^{-1} + \delta_{\text{c0}}^{-1} \right]^{-1}$ and the characteristic height of the meniscus $H_{\text{ch}} = \left[(S/2)^{-1} + (l_{\text{ch}})^{-1} \right]^{-1}$. The length of the intrinsic meniscus (l_{ch}) is defined as a multiple of δ_{ch} , and the multiplication factor $l_{\text{ch}} = 5\delta_{\text{c0}}$ is found based on calibration against the evaporation model developed in Section 2.1 for a range of structure length scales and contact angles. The thin-film characteristic thickness-to-height ratio can be calculated as

$$\frac{\delta_{\text{ch}}}{H_{\text{ch}}} = \frac{\left[(S/2)^{-1} + \delta_{\text{c0}}^{-1} \right]^{-1}}{\left[(S/2)^{-1} + (5\delta_{\text{c0}})^{-1} \right]^{-1}} \quad (11)$$

The above formula neglects the influence of contact angle and structure curvature on the thin-film characteristics. However, the inclusion of such effects would compromise the simplicity of the FOM. For the reader's interest, an extension of the formulation is presented in the supplemental material S3 that also captures the influence of contact angle and structure curvature.

3. Results and Discussion

3.1 Comparison of the evaporation model with the figure of merit (FOM)

The figure of merit (FOM) developed above is compared against the evaporation model (Section 2.1). Figure 4 (a) presents the heat flux predictions of the three different structured surfaces considered using the evaporation model. The pitch of the structured surfaces is held constant at 20 μm and their diameter-to-pitch ratio is changed to vary the porosity. The model is solved at a surface superheat of 2.5 $^{\circ}\text{C}$ for water at a saturation temperature of 298K with an

accommodation coefficient of $\hat{\sigma} = 0.3$. The thermophysical properties used to compare against different studies are provided in the supplemental material S4. Figure 4 (b) presents the calculated FOM for these structures. Note that the evaporation model for heat flux (W/cm^2) and the figure of merit (dimensionless) have different units.

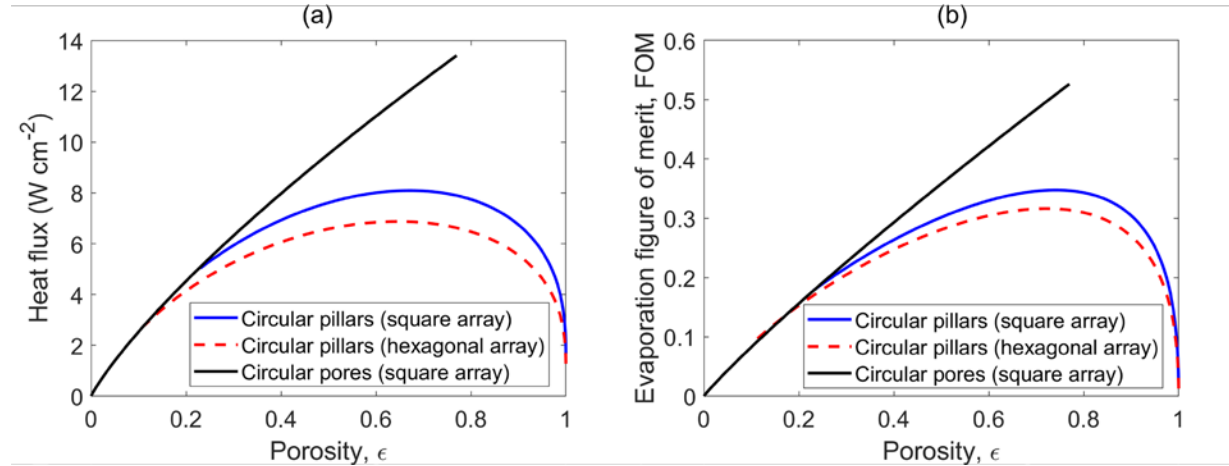


Figure 4. Prediction of evaporative performance of square array pillars, hexagonal array pillars, and square pore array structures. The porosity is varied by changing the diameter-to-pitch ratio while keeping the pitch constant at $P = 20 \mu\text{m}$ and contact angle $\theta = 60^\circ$: (a) heat flux predicted by the evaporation model; and (b) the figure of merit (FOM).

A comparison of Figure 4 (a) and (b) reveals that the figure of merit appropriately captures the trends in the heat flux for the different array morphologies and parameters for these three different structures. Circular pores (square array) exhibit an increase in heat flux with porosity. At a given pitch, increasing the pore diameter increases the three-phase contact line length and the effective area available for evaporation. Both changes help to increase the evaporative heat transfer from the surface. In contrast, the performance of the pillar arrays is non-monotonic. At low porosities, the area available for evaporation is very low; as the porosity is increased the available area of evaporation increases, but the three-phase contact line length per unit area decreases. These opposing trends give rise to a non-monotonic variation in the heat flux with porosity in the pillared structures. The figure of merit captures these essential trends; specifically, the monotonic and non-monotonic nature of the porosity dependence is captured for both pore and pillared structures, respectively. Additionally, the optimum porosity for the square pillar array and hexagonal pillar array are respectively predicted to be 0.67 and 0.65 based on the evaporation model. The FOM for these structures predicts optima of 0.74 and 0.73, respectively, within 13% of the evaporation

model predictions for this case. Furthermore, the FOM captures the relative evaporative heat transfer performance across different structure types. For instance, according to the evaporation model in Figure 4 (a), at a given porosity, the circular pore (square array) is predicted to perform better than the hexagonal pillar array, followed by the square pillar array. This same sequence is captured by the figure of merit in Figure 4 (b).

Ideally, a figure of merit for evaporative heat transfer would have a directly proportional correlation to the predicted heat fluxes. To verify that this is true of the proposed FOM, the evaporation FOM obtained for the different structures at various porosities is plotted in Figure 5 against their respective heat flux dissipation rates predicted by the evaporation model. The data collapse into a nearly linear correlation between the heat flux and FOM. An important observation is that this linear correlation is independent of the morphology of the structure used. The generalized figure of merit formula given by Equation (10) depends solely on the three-phase contact line length per unit area, the effective area of evaporation, characteristic dimensions of the thin liquid film and liquid properties. All these parameter groupings can be generally defined for any structure type, which allows for its application across different morphological structures. Comparison to data in the literature for additional structures is considered in the next section.

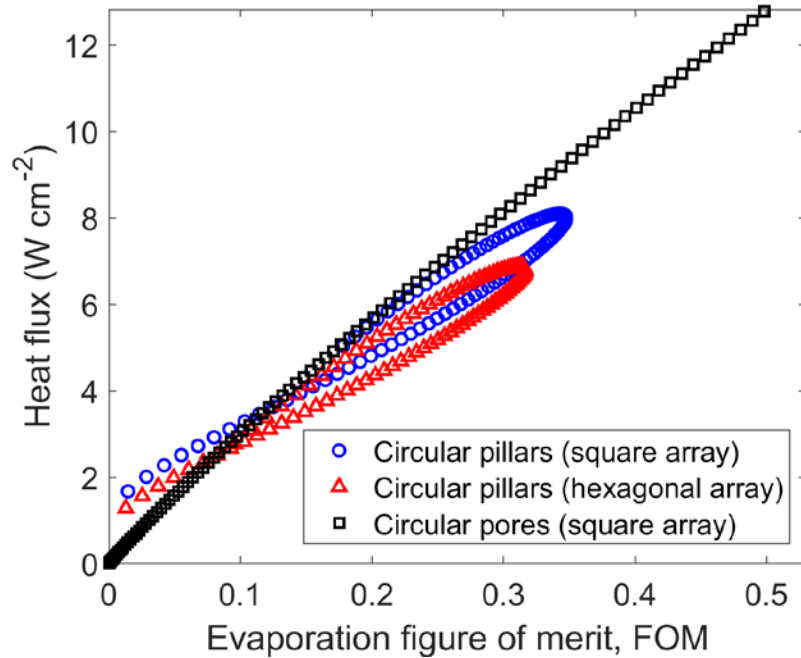
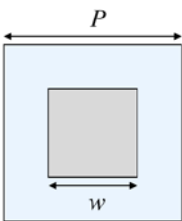
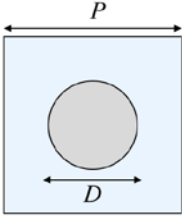


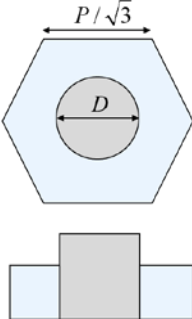
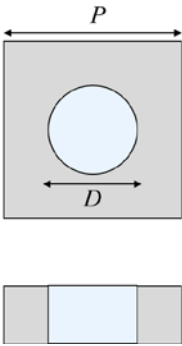
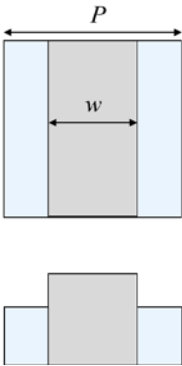
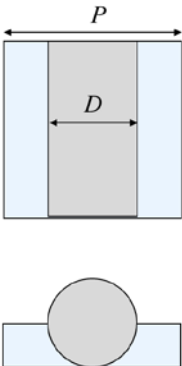
Figure 5. Heat flux predicted by the evaporation model (Figure 4a) is plotted against the figure of merit (Figure 4b) for circular pillars (square array), circular pillars (hexagonal array), and circular pores (square array).

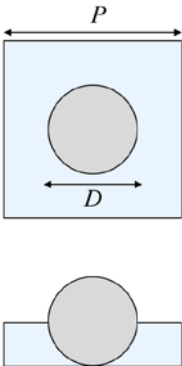
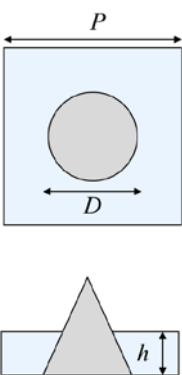
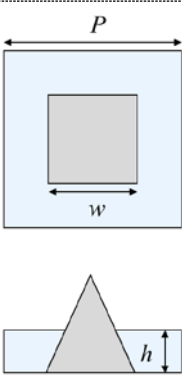
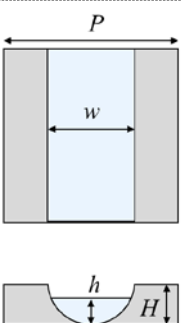
3.2 Comparison of the figure of merit (FOM) with data from the literature

In this section, we show the FOM is valid for assessing the evaporation performance trends across different structures surveyed in the literature. Extant evaporative heat transfer performance data are collected from experimental, numerical, and analytical studies. Among the many previous studies, the comparison is restricted to studies of evaporation from microstructured surfaces (length scale on the order of $\sim 1 \mu\text{m}$ to $\sim 1000 \mu\text{m}$) to a saturated vapor ambient from a static meniscus. This narrows the available results to those from Ranjan et al. ([26], [27]), Montazeri et al. [31], and Farokhnia et al. [29]. Expressions for the parameters required to calculate the FOM for the different microstructure morphologies are given in Table 1.

Table 1. Expressions for parameter groupings for different microstructured surfaces.

Structure type	Unit cell top view and side view	Porosity (ε)	$\frac{L_{cl}}{A_{fp}}$	$\frac{A_{evap}}{A_{fp}}$
Square pillars (square array)		$1 - \left(\frac{w}{P}\right)^2$	$\frac{4w}{P^2}$	$\frac{2\varepsilon}{1 + \sin \theta}$
Circular pillars (square array)		$1 - \frac{\pi}{4} \left(\frac{D}{P}\right)^2$	$\frac{\pi D}{P^2}$	$\frac{2\varepsilon}{1 + \sin \theta}$

Structure type	Unit cell top view and side view	Porosity (ε)	$\frac{L_{cl}}{A_{fp}}$	$\frac{A_{evap}}{A_{fp}}$
Circular pillars (hex array)		$1 - \frac{1}{2\sqrt{3}} \left(\frac{D}{P} \right)^2$	$\frac{2\pi D}{\sqrt{3}P^2}$	$\frac{2\varepsilon}{1 + \sin \theta}$
Circular pores (square array)		$\frac{\pi}{4} \left(\frac{D}{P} \right)^2$	$\frac{\pi D}{P^2}$	$\frac{2\varepsilon}{1 + \sin \theta}$
Rectangular ribs		$1 - \left(\frac{w}{P} \right)$	$\frac{2}{P}$	$\frac{\varepsilon \left(\frac{\pi}{2} - \theta \right)}{\cos \theta}$
Circular ribs		$1 - \left(\frac{D}{P} \right)$	$\frac{2}{P}$	$\frac{\varepsilon \left(\frac{\pi}{2} - \theta \right)}{\cos \theta}$

Structure type	Unit cell top view and side view	Porosity (ε)	$\frac{L_{cl}}{A_{fp}}$	$\frac{A_{evap}}{A_{fp}}$
Packed Sphere array (square)		$1 - \frac{\pi}{4} \left(\frac{D}{P} \right)^2$	$\frac{\pi D}{P^2}$	$\frac{2\varepsilon}{1 + \sin \theta}$
Conical structures (square packed)		$1 - \left[\pi \frac{R^2}{P^2} \left(1 - \frac{h}{H} \right)^2 \right]$ *h is the meniscus height	$\frac{2\pi R}{P^2} \left(1 - \frac{h}{H} \right)$	$\frac{2\varepsilon}{1 + \sin \theta}$
Pyramidal structures (square packed)		$1 - \left[\frac{W}{P} \left(1 - \frac{h}{H} \right) \right]^2$ *h is the meniscus height	$\frac{4W}{P^2} \left(1 - \frac{h}{H} \right)$	$\frac{2\varepsilon}{1 + \sin \theta}$
Horizontal cylindrical grooves		$\frac{2}{P} \sqrt{R^2 - (H - h)^2} = 2R / P$ *h (meniscus height) is taken to be the height of the structure	$2 / P$	$\varepsilon \left(\frac{\pi - \theta}{2 \cos \theta} \right)$

The influence of dimensional parameter variations, such as porosity and size of the surface structures, on the FOM are compared with literature [26, 29]. Comparison of trends predicted by the figure of merit against the results of Farokhnia et al. [29], who explored the influence of porosity on the evaporative performance of square pillars (square array), circular pillars (square array), and rectangular ribs, is presented in Figure 6 a-c. The left vertical axis (blue) is the heat flux from Ref. [29] plotted as a function of porosity on the horizontal axis, and the FOM is plotted on the right vertical axis (orange). The pitch here is fixed at 100 μm and the diameter/width of the structures are varied to obtain different porosities. The heat flux for both circular and square pillars shows a nonmonotonic trend with porosity. As discussed in Section 3.1, there is an optimum value of porosity due to the tradeoff between the effective area and the three-phase contact line per unit length. The FOM finds excellent agreement with the optimum porosity predicted for square and circular pillars at a given pitch. Figure 6 d represents the influence of the circular rib diameter on the FOM at a fixed porosity (0.56), and its comparison to evaporation heat flux data from Ref. [26]. The FOM captures the sharp reduction in the evaporative heat flux when the size of the structure is increased. These plots confirm that the FOM captures the trends predicted by these higher-fidelity models from the literature and can be used to identify the optimal structures.

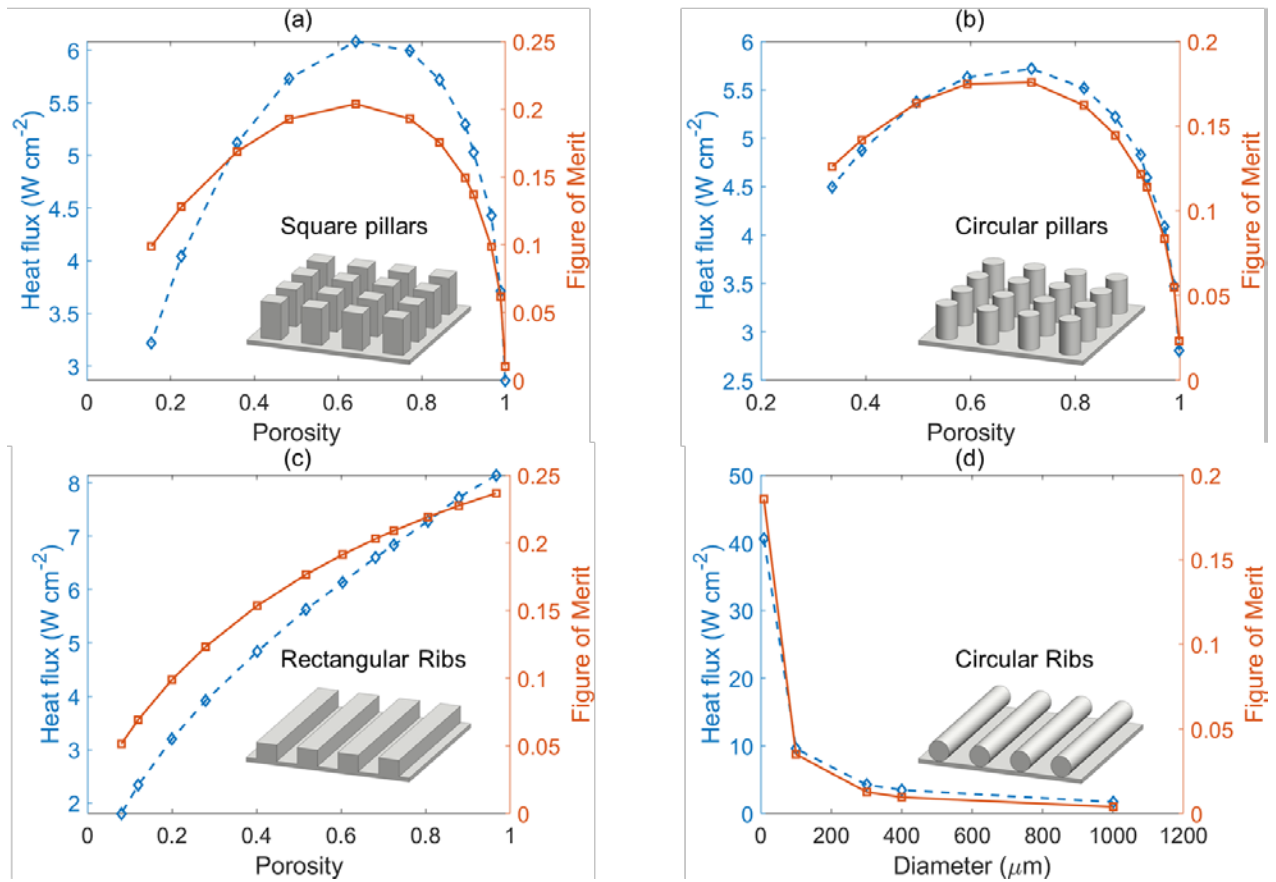


Figure 6. Heat flux data from the literature (left vertical axis; blue) along with the figure of merit (right vertical axis; orange) plotted against porosity for (a) square pillars (square array), (b) circular pillars (square array), and (c) rectangular ribs, as well as with (d) varying diameter circular ribs. The literature heat flux data for (a)-(c) are from Ref. [29], and for (d) from Ref. [26].

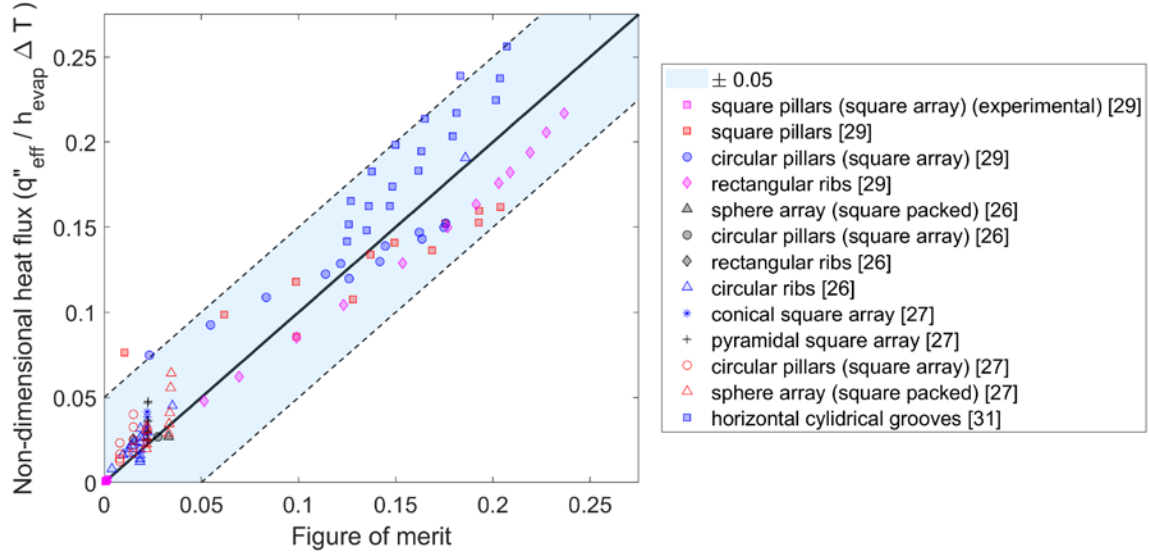


Figure 7. Non-dimensional evaporation heat flux results for structured surfaces from Refs. [26], [27], [29], and [31] are plotted against the figure of merit (FOM) developed in the present work. The solid black line represents $q''_{\text{eff}}/h_{\text{evap}}\Delta T = FOM$.

A comparison of the FOM value versus the heat flux predicted or measured in the literature [26, 27, 29, 31] for different structures is presented in Figure 7. The heat flux is non-dimensionalized as $q''_{\text{eff}}/(h_{\text{evap}}\Delta T)$ to collapse the data from studies featuring different superheats, fluids, and other boundary conditions. The figure of merit has a close linear correlation with non-dimensional heat flux obtained from the literature with an R-squared value of 0.91 across the 113 data points presented in Figure 7. The figure of merit effectively captures the evaporative heat transfer performance of different structures in the literature including a wide range of sizes (pitches from $17.82\ \mu\text{m}$ to $17.85\ \text{mm}$) and porosities (0.15 to 1). One exception is the influence of the contact angle which leads to a higher deviation for a particular dataset near the origin for non-prismatic structures and circular pillars (from Ref. [27]). This dataset corresponds to heat flux predictions for a given structured surface at different contact angles. The influence of contact angle is only accounted for in the FOM through the calculation of the effective area of evaporation, but as noted earlier in Section 2.2, the contact angle can impact the thin-film characteristics as well. We introduce an alternative approach for determining thin-film characteristics accounting for the contact angle in the supplemental material S3, which improves the prediction performance, but compromises the simplicity of the thin-film characteristics given by Equation (11). For surveying

the different available structure geometries, for a fixed solid-liquid combination, the thin-film characteristics ($\delta_{\text{ch}}/H_{\text{ch}}$) calculated using Equation (11) would result in accurate quantitative variations in FOM. For improved predictions accounting for the influence of contact angle, and for the cases of non-prismatic structures, a higher fidelity approach for the calculation of the thin-film characteristics is provided in the supplemental material S3.

The above comparison with the data in the literature suggests that the FOM is an effective tool for assessment of structured surfaces. The validation of trends for pillar and pore structures (Figure 4) shows that the FOM is very useful in predicting the trends of evaporative heat flux for a given structured surface type. However, due to the necessary simplifications and assumptions required to arrive at the structure-agnostic parameter groupings comprising the FOM, it is expected that it does not have perfect accuracy in predicting the evaporative heat flux, and some spread in the data is observed in Figure 7. For comparison across different surfaces, a spread of ± 0.05 in non-dimensional heat flux prediction is expected as observed in Figure 7.

3.3 Implications of the figure of merit (FOM) on evaporation enhancement

This section discusses the key parameter groupings identified in the formulation of the figure of merit, and offers guidance for obtaining enhanced evaporation from microstructured surfaces.

1. A larger three-phase contact line length per unit footprint area ($L_{\text{cl}}/A_{\text{fp}}$) of a structure is desired. This suggests smaller structures and a higher packing density of the contact line.
2. A larger meniscus area per unit footprint area ($A_{\text{evap}}/A_{\text{fp}}$) is beneficial. Thus, surfaces with high 2D porosities as well as low contact angles (low contact angles increase the curvature and area of the meniscus) support superior performance.
3. Heat transfer performance generally increases with a decrease in the scale of the microstructure. Smaller-scale structures (compared to larger-scale structures) have a higher three-phase contact line length per unit area ($L_{\text{cl}}/A_{\text{fp}}$) while maintaining the same effective area ($A_{\text{evap}}/A_{\text{fp}}$) available for evaporation. However, it is important to note that smaller length scales increase the challenge of sustaining liquid feeding due to their lower permeability, a factor that must be considered outside of this evaporation model. Hierarchical structures can help resolve such challenges.

4. Low contact angle surfaces are desired as they increase the meniscus curvature, leading to a higher area available for evaporation ($A_{\text{evap}}/A_{\text{fp}}$). Lower contact angles also provide better thin-film properties (lower thickness δ_{ch} and larger meniscus height H_{ch}).
5. Structures that increase the height of the thin-film area (H_{ch}) and decrease the characteristic thickness (δ_{ch}) of the thin-film area lead to better evaporation heat transfer. Unique structures such as inverse opals, catenoids, and horizontal cylindrical grooves can enhance the length of the thin-film region. Such structures have a high effective length to meniscus thickness ratio.
6. For a given morphology, variation of the different feature sizes can lead to a tradeoff between the properties governing the evaporation enhancement ($L_{\text{cl}}/A_{\text{fp}}$, $A_{\text{evap}}/A_{\text{fp}}$, $\delta_{\text{ch}}/H_{\text{ch}}$). For instance, in Figure 6 a-b, a change in porosity causes competition between the area available for evaporation ($A_{\text{evap}}/A_{\text{fp}}$) and the three-phase contact line length per unit area ($L_{\text{cl}}/A_{\text{fp}}$), leading to the existence of an optimum in evaporation heat flux.
7. For a given solid-liquid combination, the evaporation performance can further be affected by changes in the contact angle that can arise from wetting hysteresis. The FOM predicts the evaporative performance for a specified contact angle, but in practice any contact angle hysteresis could lead to a range of evaporative performance. Such variation in evaporative performance due to contact angle hysteresis has been experimentally observed [32] and should be carefully considered for evaporative structure design

4. Conclusions

In this work, we introduced a figure of merit (FOM) for the evaporation heat transfer from microstructured surfaces. The FOM was calibrated against a higher-fidelity evaporation model for circular pillars in square and hexagonal arrays and circular pores in a square array. The figure of merit identified four important parameter groupings that affect the evaporative heat flux: (i) the three-phase contact line length per unit area $L_{\text{cl}}/A_{\text{fp}}$; (ii) a thermophysical property constant k_1/h_{lv} ; (iii) the effective area of evaporation $A_{\text{evap}}/A_{\text{fp}}$; and (iv) the characteristic dimensions of the liquid thin film $\delta_{\text{ch}}/H_{\text{ch}}$. Methods for estimating all the structure-agnostic parameter

groupings governing the FOM were provided. A comparison of the heat flux predictions from the literature with the FOM developed here showed a strong linear correlation. The influence of the key parameter groupings was analyzed to obtain microstructure design guidelines for maximizing evaporation heat transfer performance. The figure of merit serves as an effective tool to assess evaporative heat transfer performance across different structure morphologies and to obtain optimum structure dimensions.

Acknowledgments

This work was supported in part by Purdue's NEPTUNE Center for Power and Energy, funded by the Office of Naval Research under Grant No. N000141613109. This work used the Extreme Science and Engineering Discovery Environment (XSEDE), which is supported by the National Science Foundation grant number ACI-1548562.

Appendix A. Supplementary material

Supplementary data associated with this article can be found in the online version.

References

- [1] X. Chen, D. Goodnight, Z. Gao, A.H. Cavusoglu, N. Sabharwal, M. DeLay, A. Driks, O. Sahin, Scaling up nanoscale water-driven energy conversion into evaporation-driven engines and generators, *Nature Communications*. 6 (2015) 7346.
- [2] O.K. Varghese, M. Paulose, T.J. LaTempa, C.A. Grimes, High-rate solar photocatalytic conversion of CO₂ and water vapor to hydrocarbon fuels, *Nano Letters*. 9 (2009) 731–737.
- [3] P. Yang, K. Liu, Q. Chen, J. Li, J. Duan, G. Xue, Z. Xu, W. Xie, J. Zhou, Solar-driven simultaneous steam production and electricity generation from salinity, *Energy & Environmental Science*. 10 (2017) 1923–1927.
- [4] H. Ghasemi, G. Ni, A.M. Marconnet, J. Loomis, S. Yerci, N. Miljkovic, G. Chen, Solar steam generation by heat localization, *Nature Communications*. 5 (2014) 4449.
- [5] G. Ni, G. Li, S.V. Boriskina, H. Li, W. Yang, T. Zhang, G. Chen, Steam generation under one sun enabled by a floating structure with thermal concentration, *Nature Energy*. 1 (2016) 1–7.
- [6] X. Li, W. Xu, M. Tang, L. Zhou, B. Zhu, S. Zhu, J. Zhu, Graphene oxide-based efficient and scalable solar desalination under one sun with a confined 2D water path, *Proceedings of the National Academy of Sciences*. 113 (2016) 13953–13958.
- [7] P. Zhu, T. Kong, C. Zhou, L. Lei, L. Wang, Engineering microstructure with evaporation-induced self-assembly of microdroplets, *Small Methods*. 2 (2018) 1800017.

- [8] A. Kampl, Bitcoin 2-Phase Immersion cooling and the implications for high performance computing, *Electronics Cooling Magazine*. (2014) 1.
- [9] P.A. de Oliveira, J.R. Barbosa, Novel two-phase jet impingement heat sink for active cooling of electronic devices, *Applied Thermal Engineering*. 112 (2017) 952–964.
- [10] K.P. Drummond, D. Back, M.D. Sinanis, D.B. Janes, D. Peroulis, J.A. Weibel, S.V. Garimella, A hierarchical manifold microchannel heat sink array for high-heat-flux two-phase cooling of electronics, *International Journal of Heat and Mass Transfer*. 117 (2018) 319–330.
- [11] B.V. Deryagin, S.V. Nerpin, N.V. Churaev, To the theory of liquid evaporation from capillaries, *Kolloidnyi Zhurnal* 26 (1964) 301–307.
- [12] P.C. Wayner, Interfacial profile in the contact line region of a finite contact angle system, *Journal of Colloid and Interface Science*. 77 (1980) 495–500.
- [13] H. Wang, S.V. Garimella, J.Y. Murthy, Characteristics of an evaporating thin film in a microchannel, *International Journal of Heat and Mass Transfer*. 50 (2007) 3933–3942.
- [14] C. Yan, H.B. Ma, Analytical Solutions of heat transfer and film thickness in thin-film evaporation, *Journal of Heat Transfer*. 135 (2013).
- [15] V.S. Ajaev, J. Klentzman, C. Sodtke, P. Stephan, Mathematical modeling of moving contact lines in heat transfer applications, *Microgravity Science and Technology*. 19 (2007) 23–26.
- [16] K. Ibrahim, M.F. Abd Rabbo, T. Gambaryan-Roisman, P. Stephan, Experimental investigation of evaporative heat transfer characteristics at the 3-phase contact line, *Experimental Thermal and Fluid Science*. 34 (2010) 1036–1041.
- [17] C.P. Migliaccio, H.K. Dhavaleswarapu, S.V. Garimella, Temperature measurements near the contact line of an evaporating meniscus V-groove, *International Journal of Heat and Mass Transfer*. 54 (2011) 1520–1526.
- [18] R. Raj, C. Kunkelmann, P. Stephan, J. Plawsky, J. Kim, Contact line behavior for a highly wetting fluid under superheated conditions, *International Journal of Heat and Mass Transfer*. 55 (2012) 2664–2675.
- [19] S.C. Maroo, J.N. Chung, Heat transfer characteristics and pressure variation in a nanoscale evaporating meniscus, *International Journal of Heat and Mass Transfer*. 53 (2010) 3335–3345.
- [20] S. Narayanan, A.G. Fedorov, Y.K. Joshi, Interfacial Transport of Evaporating Water Confined in Nanopores, *Langmuir*. 27 (2011) 10666–10676.
- [21] J.L. Plawsky, A.G. Fedorov, S.V. Garimella, H.B. Ma, S.C. Maroo, L. Chen, Y. Nam, Nano- and microstructures for thin-film evaporation—A review, *Nanoscale and Microscale Thermophysical Engineering*. 18 (2014) 251–269.
- [22] Y.X. Wang, G.P. Peterson, Analytical model for capillary evaporation limitation in thin porous layers, *Journal of Thermophysics and Heat Transfer*. 17 (2003) 145–149.
- [23] C. Li, G.P. Peterson, Y. Wang, Evaporation/Boiling in thin capillary wicks (I)—Wick thickness effects, *Journal of Heat Transfer*. 128 (2006) 1312–1319.
- [24] C. Li, G.P. Peterson, Evaporation/Boiling in thin capillary wicks (II)—Effects of volumetric porosity and mesh size, *Journal of Heat Transfer*. 128 (2006) 1320–1328.
- [25] M.A. Hanlon, H.B. Ma, Evaporation heat transfer in sintered porous media, *Journal of Heat Transfer*. 125 (2003) 644–652.
- [26] R. Ranjan, J.Y. Murthy, S.V. Garimella, A microscale model for thin-film evaporation in capillary wick structures, *International Journal of Heat and Mass Transfer*. 54 (2011) 169–179.

- [27] R. Ranjan, A. Patel, S.V. Garimella, J.Y. Murthy, Wicking and thermal characteristics of micropillared structures for use in passive heat spreaders, *International Journal of Heat and Mass Transfer*. 55 (2012) 586–596.
- [28] K.K. Bodla, J.Y. Murthy, S.V. Garimella, Evaporation analysis in sintered wick microstructures, *International Journal of Heat and Mass Transfer*. 61 (2013) 729–741.
- [29] N. Farokhnia, P. Irajizad, S.M. Sajadi, H. Ghasemi, Rational Micro/Nanostructuring for Thin-Film Evaporation, *The Journal of Physical Chemistry C*. 120 (2016) 8742–8750.
- [30] S. Adera, D. Antao, R. Raj, E.N. Wang, Design of micropillar wicks for thin-film evaporation, *International Journal of Heat and Mass Transfer*. 101 (2016) 280–294.
- [31] K. Montazeri, H. Lee, Y. Won, Microscopic analysis of thin-film evaporation on spherical pore surfaces, *International Journal of Heat and Mass Transfer*. 122 (2018) 59–68.
- [32] S. Bang, S. Ryu, S. Ki, K. Song, J. Kim, J. Kim, Y. Nam, Superhydrophilic catenoidal aluminum micropost evaporator wicks, *International Journal of Heat and Mass Transfer*. 158 (2020) 120011.
- [33] R.W. Schrage, *A Theoretical Study of Interphase Mass Transfer*, Columbia University Press, 1953.
- [34] V.P. Carey, *Liquid-Vapor Phase-Change Phenomena: An Introduction to The Thermophysics of Vaporization and Condensation Processes in Heat Transfer Equipment*, CRC Press, 2020.